J Therm Anal Calorim (2010) 100:733–740
DOI 10.1007/s10973-009-0209-y

Oxidation kinetics of nickel nano crystallites obtained by controlled thermolysis of diaquabis(ethylenediamine) nickel(II) nitrate

Ponminiessary P. Robinson · Vasudevan Arun · Sebastian Manju · Chennampilly Ummer Aniz · Karukapadath K. M. Yusuff

Received: 3 April 2009 / Accepted: 5 June 2009 / Published online: 8 July 2009

Abstract The metal complex, $[Ni(en)_2(H_2O)_2](NO_3)_2$ (en = ethylenediamine), was decomposed in a static furnace at 200 °C by autogenous decomposition to obtain phase pure metallic nickel nanocrystallites. The nickel metal thus obtained was studied by XRD, IR spectra, SEM and CHN analysis. The nickel crystallites are in the nanometer range as indicated by XRD studies. The IR spectral studies and CHN analyses show that the surface is covered with a nitrogen containing species. Thermogravimetric mass gain shows that the product purity is high (93%). The formed nickel is stable and resistant to oxidation up to 350 °C probably due to the coverage of nitrogen containing species. Activation energy for the oxidation of the prepared nickel nanocrystallites was determined by non-isothermal methods and was found to depend on the conversion ratio. The oxidation kinetics of the nickel crystallites obeyed a Johnson–Mehl–Avrami mechanism probably due to the special morphology and crystallite strain present on the metal.

Keywords Ethylenediamine · Thermolysis · Nano nickel · Oxidation kinetics

Introduction

Nano nickel is very important in the current science as it finds applications in catalysis, magnetic recording, semiconductors and biological labeling [1–4]. There are so many methods to prepare nickel nanoparticles like sonochemical [5], reduction of nickel salts [6], carbonyl method [7] and ligand assisted synthesis [8]. There is a continuing interest in easy synthesis of metallic nano nickel. Recently, Wang et al. [9] reported the synthesis of nano nickel by thermal decomposition of nickel acetate along with a surfactant hexadecylamine. They obtained nano sized nickel (7 nm) with a product purity of approximately 74.3%.

Nickel nano particles were also obtained by controlled evaporation of nickel–oleyl amine complex solution [10]. Such preparation methods employ costly surfactants and the product is usually contaminated with organic species. Thermolysis of ethylenediamine (en) complexes usually gives NiO [11]. Recently the ethylenediamine complexes of nickel have been used in the preparation of supported nickel catalysts [12, 13]. The preparation method involves decomposition of catalyst precursors (the support and the nickel complex) in an inert atmosphere and partially reduced nickel species were obtained on the support surface.

Metals in nanometer scale have high surface area and are more probable to oxidation at a faster rate than their bulk counterparts. As the use of nano sized metals is gaining importance, their corrosion and activity loss due to oxidation is worth for studies. Oxidation kinetics of bulk nickel has been studied by Atkinson and Taylor [14]. Oxidation kinetics of nickel nanoparticles has gained renewed interest as it is a potential candidate for chemical looping combustion [15–17]. Different parameters like atmosphere, heating procedure, particle size and presence of impurities influence the oxidation behavior of nickel. The oxidation resistance of

---

Electronic supplementary material The online version of this article (doi:10.1007/s10973-009-0209-y) contains supplementary material, which is available to authorized users.

P. P. Robinson · V. Arun · S. Manju · K. K. M. Yusuff (✉)
Department of Applied Chemistry, Cochin University of Science & Technology, Kochi 682022, India
e-mail: yusuff@cusat.ac.in

C. U. Aniz
Research and Development Division, Sud Chemie India Ltd, Kochi 683502, India

nickel is important, as resistant metal will be more stable at room temperature. Size dependent kinetics for nano nickel oxidation has been studied by Karmhag et al. [18]. We have synthesized nanocrystalline nickel by simple thermal decomposition of the complex, $[Ni(en)_2(H_2O)_2](NO_3)_2$. The decomposition product was characterized by XRD, IR, SEM and elemental analysis. The oxidation kinetics of the formed nickel nanocrystallites were studied by model free and model fitting kinetics methods. The details of these studies are presented in this paper.

Experimental

Preparation of the complex

The complex, $[Ni(en)_2(H_2O)_2](NO_3)_2$ was prepared according to the reported procedure [19] by adding stoichiometric amount of ethylenediamine (2.05 g) to a solution of nickel nitrate (4.96 g) in water (50 mL) with stirring. The solution was kept in an ice bath for 4 h. The formed precipitate was then washed with dry ethanol and dried over vacuum.

Preparation of nickel nanocrystallites

The dried complex $[Ni(en)_2(H_2O)_2](NO_3)_2$ (8 g) was kept in a static furnace of dimensions 22 cm × 20 cm × 20 cm. The temperature of the furnace was increased at a rate of 5 °C min^{-1} to 200 °C, and was kept at that temperature for 2 h. The sample first melted to a black syrupy mass, which after half an hour decomposed suddenly with evolution of gases in to a fluffy material. The resultant product was stored in an inert (dry nitrogen) atmosphere.

Instrumentation

The elemental (CHN) analyses were done on a Vario elementar III analyzer. Nickel in the complex was estimated using Atomic Absorption Spectroscopy (AAS) on a Thermo Electron Corporation SOLAAR $M5Mk_2$ system. Infrared spectrum of the complex and that of metallic nickel were recorded on a Thermo Scientific–Nicolet 380 FTIR spectrometer after pelletizing in KBr. The UV–Vis spectrum of the complex was recorded on a Labomed UV–Vis spectrophotometer. X-ray diffraction patterns were recorded on Bruker model D8 (CuKα source) and X-ray line broadening analysis (XLBA) was done with the well known Scherrer equation. The size-strain deconvolution was done by Williamson–Hall plotting [20]. SEM was recorded on a Jeol JSM-6390 LA scanning electron microscope.

The TG/DTG studies were conducted on a Pyris Diamond TG of Perkin Elmer make. For the decomposition experiments of the complex, an air flow of 50 mL min^{-1} was maintained. Different heating rates were employed to study the thermolysis of the complex. During oxidation of nickel crystallites the air flow was increased to 200 mL min^{-1}. The heating rates employed were 5, 10, 15 and 20 °C min^{-1}. All the TG/DTG experiments were done at atmospheric pressure.

Results and discussion

Characterisation of the complex

The results of the elemental analysis and IR and UV–Vis spectral studies of the metal complex are summarized in the Table 1 (for the figures of IR and UV–Vis spectra see electronic supplementary material).

The analytical data and IR and UV–Vis spectroscopic data are in agreement with that for the octahedral complex, $[Ni(en)_2(H_2O)_2](NO_3)_2$, reported in the literature [21–23].

The product formed on keeping this complex at isothermal temperature (200 °C) in the static furnace for 2 h was characterized by XRD, TG, IR and SEM.

XRD analysis

XRD pattern of the product obtained is shown in Fig. 1A, which could be well indexed as face centered cubic (fcc) nickel [24].

There were no peaks due to NiO or the starting complex indicating the formation of phase pure product. The peaks were subjected to Lorentzian curve fit, and the fwhm (full width at half maximum) (τ) were determined after deducting the instrumental broadening. The lattice constant calculated from the 2θ values was 3.5192 Å. The crystallite sizes were calculated from the (111), (200) and (220) reflections by the well known Scherrer equation (for line broadening),

$$d_{\mathrm{vol}} = \frac{0.9\lambda}{\tau \cos\theta}$$

where d_{vol} is the volume average crystallite size and λ is the wavelength of X-ray and the values were 15.0, 16.1 and 9.8 nm respectively. The variation in crystallite size for different crystallographic planes indicates that the crystallite sizes and shapes are not homogeneous. The X-ray line broadening can be due to size effect or/and strain effect. We did the Williamson–Hall method to separate the strain contribution from the total fwhm. Williamson–Hall method to separate the broadening due to size and strain is based on the equation.

Table 1 Characterisation of the complex

Elemental analysis (%) Observed (calculated)				IR (cm^{-1})				UV–Vis (nm)			
Ni	C	H	N	NO_3^a	Ni–N	CH_2	H_2O^b	$\pi \to \pi^*$ NO_3	λ_1 $^3A_{2g} \to {}^3T_{2g}$	λ_2 $^3A_{2g} \to {}^3T_{1g}(F)$	λ_3 $^3A_{2g} \to {}^3T_{1g}(P)$
17.41 (17.32)	14.22 (14.17)	5.87 (5.95)	24.69 (24.80)	834, 1370, 2390, 1030	438	2878, 2934	405, 652, 3445	301	356	566	928

[a] Ionic nitrate

[b] Coordinated water

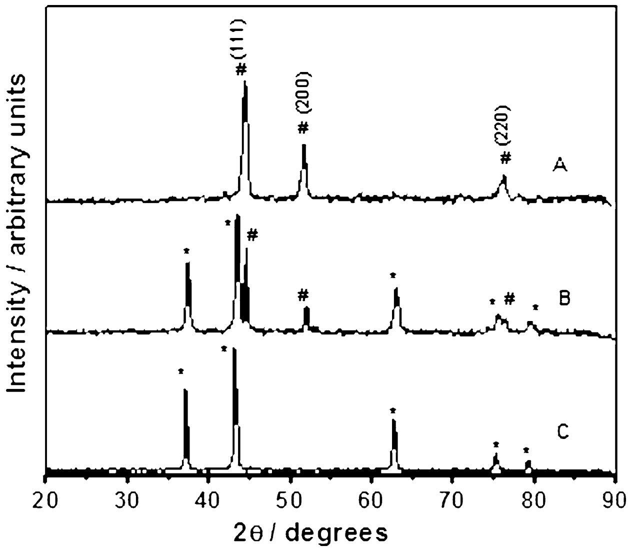

Fig. 1 X-ray diffraction pattern of *A*—phase pure nickel obtained from static furnace, *B*—intermediate separated after stage B of decomposition in TG, *C*—final product of decomposition from TG. * Peaks due to NiO, # peaks due to metallic nickel

$$\text{fwhm} = \tau_{\text{size}+\text{strain}} = \tau_{\text{size}} + \tau_{\text{strain}}$$

$$\tau_{\text{size}+\text{strain}} = \frac{K\lambda}{\cos\theta * d_{\text{vol}}} + \eta\tan\theta; \quad \text{where } \eta\tan\theta = \tau_{\text{strain}}$$

$$\tau_{\text{size}+\text{strain}} * \cos\theta = \frac{K\lambda}{d_{\text{vol}}} + \eta\sin\theta$$

where K is the shape factor usually 0.9 and η is the microstrain.

Thus a plot of $\tau_{\text{size+strain}}$ * cosθ against sinθ gives a straight line with slope η. From the y-intercept the crystallite size corrected for microstrain can be calculated.

The W–H plot for our sample is shown in Fig. 2. The calculated average crystallite size from the y-intercept of the W–H plot was 18.1 nm. This value is greater than the values calculated by usual Scherrer equation indicating considerable microstrain in our sample. The positive slope of the plot gave the microstrain ($\eta = 0.0235$) which was significant. Points not lying along the straight line indicate anisotropic strain. The XRD analysis of the sample thus indicates formation of nanocrystalline phase pure nickel with significant anisotropic microstrain.

TG, IR spectra and SEM

The mass gain (Fig. 3) observed in the TG curve due to oxidation of the nickel was 20.1% against the theoretical mass gain of 27.3% (if the product was 100% nickel).

The CHN analysis of the product yielded the results as C, 2.2; H, 1.2; and N, 5.5%. Combining both the above results, purity of the nickel metal is ≈93% which is higher than the reported values for similar preparation methods [9].

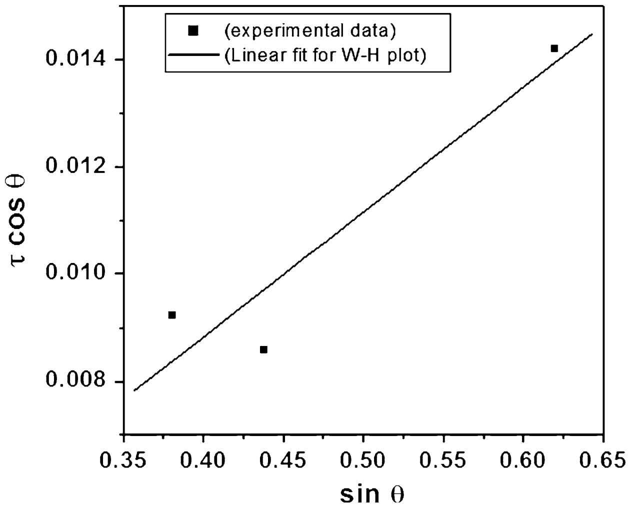

Fig. 2 Williamson–Hall plot for metallic nickel

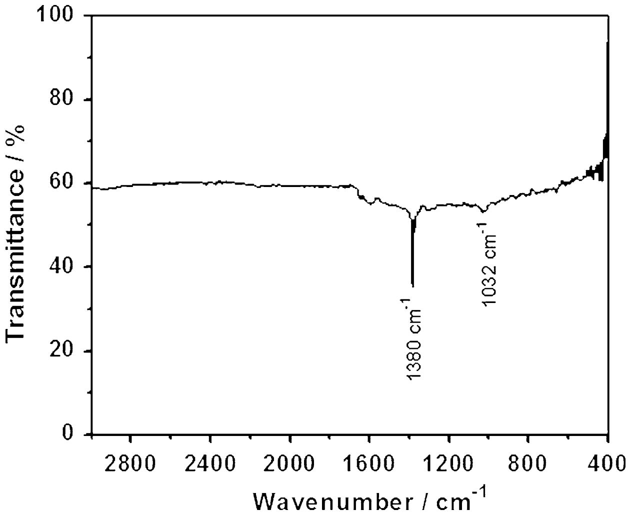

Fig. 4 IR spectra of the prepared nickel nanocrystallites

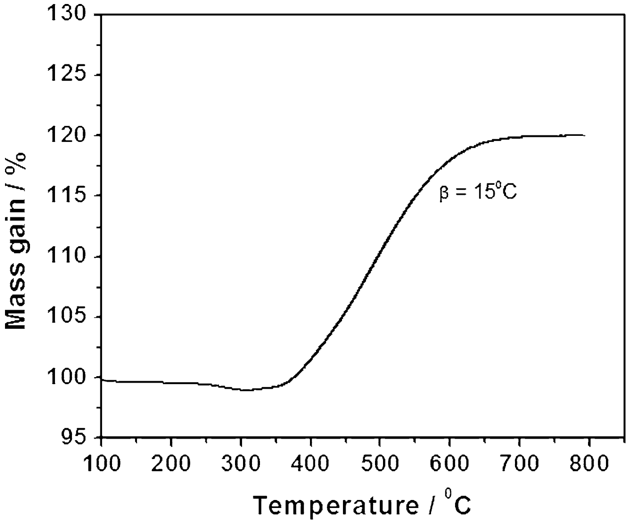

Fig. 3 The mass gain curve during oxidation

The infra-red spectrum of the product is shown in Fig. 4. The absence of Ni–O stretching vibrations in the region 420–470 cm^{-1} confirms the absence of nickel oxide formation in the product which is in accordance with the XRD results [25].

The peaks at 1,380 and 1,032 cm^{-1} may be due to the $\nu_a(NO_2)$ and $\nu_s(NO_2)$ vibrations of unidentate N-bonded nitro groups [22]. The absence of extra peaks from ligands confirms that the decomposition was almost complete. The scanning electron micrograph (Fig. 5) shows foam like structure which has been formed by the aggregation of nickel crystallites. The foam has been made up of thin film like structures.

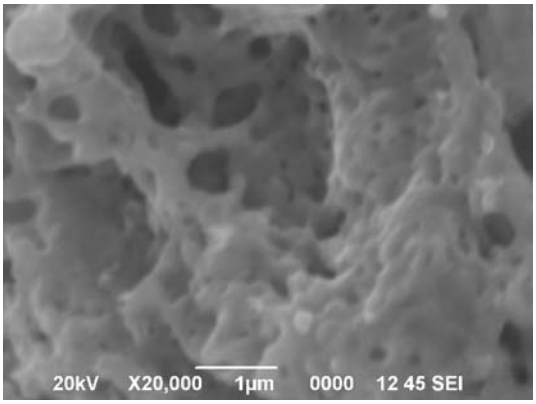

Fig. 5 SEM of metallic nickel

The temperature of decomposition in our experiment (200 °C) is less than the real decomposition temperature of the complex (240 °C). The decomposition procedure (heating rate and temperature) is important as lower temperatures yield a black charred mass, while higher temperatures result in partial formation of nickel oxide. We tried to simulate the formation of nickel crystallites in static furnace by carrying out TG runs as described below.

Thermolysis experiments

In one TG run, the nickel complex was heated from room temperature to 200 °C at a rate of 5° min^{-1} and was maintained at 200 °C for 3 h with an air flow of 50 mL min^{-1} (Fig. 6A). Even after 3 h the product obtained from TG was a black mass corresponding to a percentage mass loss of 47.7.

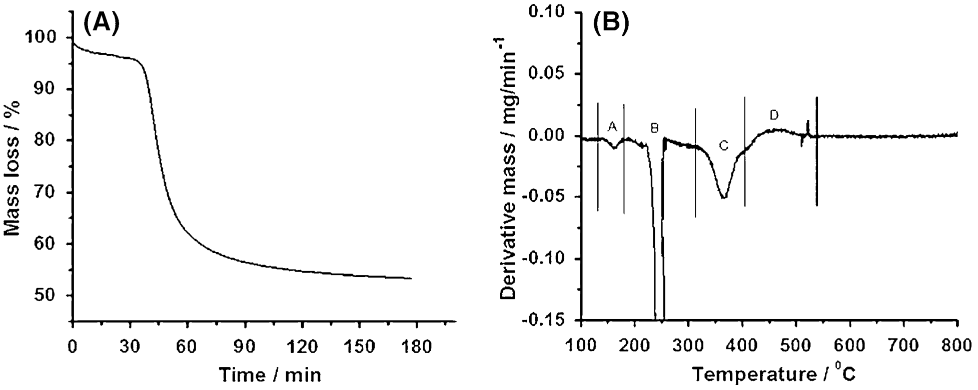

Fig. 6 **A** isothermal weight loss of $[Ni(en)_2(H_2O)_2](NO_3)_2$ at 200 °C, **B** DTG graph of thermolysis of $[Ni(en)_2(H_2O)_2](NO_3)_2$ (TG program; air flow = 50 mL min^{-1}; temperature 100 °C → 240 °C at a rate 5 °C min^{-1}; isothermal at 240 °C for 1 h; 240 °C → 800 °C at a rate of 10 °C min^{-1})

$$\left[Ni(en)_2(H_2O)_2\right](NO_3)_2 \xrightarrow{\text{in TG furnace } 200\,^{\circ}\text{C isothermal}} \text{gaseous products} + \text{partially decomposed product.}$$

We did another TG run with a heating program (air flow = 50 mL min^{-1}; temperature 100 °C → 240 °C at a rate of 5 °C min^{-1}; isothermal at 240 °C for 1 h; 240 °C → 800 °C at a rate of 10 °C min^{-1}). Our DTG results (Fig. 6B) in air atmosphere shows four stages of mass loss/gain. Stage A corresponds with mass loss of water, stage B corresponds to explosive decomposition, stage C corresponds to mass loss and reduction of Ni^{2+} and stage D corresponds to mass gain due to nickel oxidation. We isolated the product after the stage B and its XRD is shown in Fig. 1B. It showed characteristic reflections due to Ni and NiO.

The CHN elemental analyses (C, 8.1; H, 4.6; and N, 1.5 mass%) indicated the formation of a carbon rich contaminant on the surface. The mass loss around 350 °C (stage C) can be due to decomposition of carbon remains along with evolution of hydrogen [19]. The mass increase between 400 and 550 °C (stage D) is due to nickel oxidation. The XRD pattern of the final product after stage D suggests the formation of phase pure NiO (Fig. 1C) [26]. The elemental analysis (CHN < 0.5 mass%) of final product showed practically no contaminants.

Thus decomposition in stage A and B can be written as

$$\begin{aligned}\left[Ni(en)_2(H_2O)_2\right](NO_3)_2 &\xrightarrow{\text{in TG furnace } 100\text{–}240\,^{\circ}\text{C}} Ni^0 + NiO \\ &+ \text{carbon containing contaminants } (13.2\%) \\ &+ \text{gaseous products.}\end{aligned}$$

and in stage C and D as

$$\begin{aligned}&Ni^0 + NiO + \text{Carbon containing contaminants} + O_{2(TGgas)} \\ &\xrightarrow{\text{in TG furnace } 240\text{–}800\,^{\circ}\text{C}} NiO + \text{gaseous products.}\end{aligned}$$

Thus we could not observe the formation of phase pure nickel metal in the temperature range 200–240 °C in the thermolysis experiments done in TG furnace. The preparation of nickel nanocrystallites was done by isothermal decomposition in a muffle furnace with the dimensions 22 cm × 20 cm × 20 cm using a sample mass of 8 g. Partial decomposition of ethylenediamine ligands by nitrate ions/oxygen (present initially in small amount) occurs as the first step of the isothermal decomposition. The high sample/space in furnace and the partial decomposition creates an atmosphere devoid of air around the sample which prevents the formation of NiO. We propose an autogenous temperature increase in static furnace due to the partial oxidation of ethylenediamine ligands. This temperature rise initiates a self-propagating reaction by which all the ligands are decomposed to gaseous products including hydrogen, which act as reducing agents for the complete reduction of Ni^{2+} to $Ni^0_{(metal)}$. This might be the reason for the formation of nickel metal.

$$\begin{aligned}\left[Ni(en)_2(H_2O)_2\right](NO_3)_2 + O_{2(atmos)} &\xrightarrow{\text{in static furnace } 200\,^{\circ}\text{C}} \\ &Ni^0 + H_2(g) + \text{other gaseous products} \\ &+ \text{contaminants } (8.9\%).\end{aligned}$$

This direct transformation of the metal complex at low temperature to nanocrystallites of nickel is interesting as the preparation route is simple.

Oxidation of nickel nanocrystallites

The unusual morphology of the sample (thin film like three dimensional structure) prompted us to study the kinetics of oxidation of the material. The differential thermogravimetric (DTG) plots for the oxidation of metallic nickel (product obtained from the static furnace) at various heating rates are shown in the Fig. 7. There was an initial mass loss of around 0.3% near 300 °C, which is due to the combustion of contaminants covering the surface. This mass loss was deducted before the kinetics calculations were made. The conversion ratios at given temperatures are

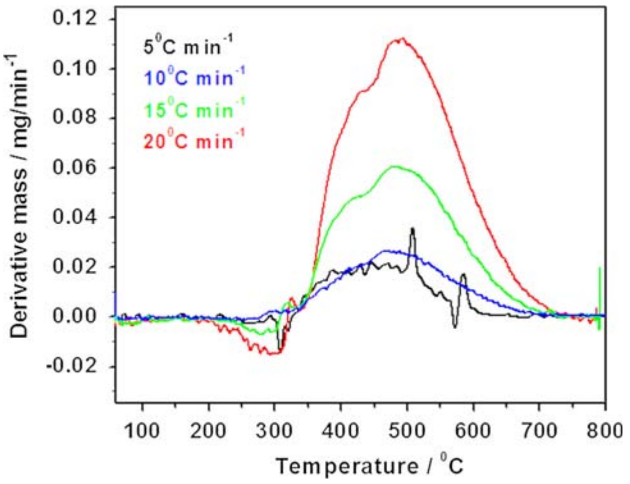

Fig. 7 DTG plot of nickel oxidation at different heating rates

determined from the TG data by assuming stoichiometric oxidation reaction. We did not consider any oxide layer if initially present on the surface and took sample mass as that of pure nickel. Complete oxidation was assumed at the attainment of maximum mass.

The mass increase due to oxidation of nickel started in between 320 and 360 °C depending on the heating rates. This temperature of initial oxidation is less compared to bulk Ni oxidation values and is attributed to the nano scale dimensions of the sample [27]. The temperature of peak maximum in the DTG plot shifted to higher values when the heating rate was increased.

Oxidation kinetics

Determination of activation energy by model-free isoconversional methods and Kissinger method

The basic assumption of model-free isoconversional methods is that the reaction rate at a constant conversion is only a function of temperature, and that the reaction model is not dependent on temperature or heating rate. Flynn–Wall–Osawa (FWO) [28] and Kissinger–Akahira–Sunose (KAS) [29] equations are generally used to study the kinetics of solid state reactions. This method allows the estimation of activation energy without choosing a reaction model and reaction order. The FWO equation in its differential form is as below.

$$\frac{d\ln\beta}{d(1/T)} = \frac{1.052 * E_a}{R};$$

where β is the linear heating rate, E_a the activation energy and R is the gas constant.

The method is based on measurement of temperatures for each conversion degree α and different heating rates β. The plots of ln β versus $1/T$ at constant α will give straight line and from the slope activation energies are determined.

The integral form of KAS equation is

$$\ln\left(\frac{\beta}{T^2}\right) = \ln\frac{A}{E_a * g(\alpha)} - \frac{E_a}{RT}$$

where A is the Arrhenius frequency factor and $g(\alpha)$ is the mechanism function.

A plot of $\ln\left(\frac{\beta}{T^2}\right)$ against $1/T$ gives a straight line with slope $= -\frac{E_a}{R}$.

Friedman differential method [30] is based on the intercomparison of the rates of conversion, dα/dT for a given degree of conversion α, at different heating rates. This method requires measurement of both temperatures and conversion rates, at different heating rates.

$$\ln\left(\beta\frac{\mathrm{d}\alpha}{\mathrm{d}T}\right) = \ln[Af(\alpha)] - \frac{E_a}{RT}$$

The activation energies were calculated by the above three equations and are plotted against each conversion degree (Fig. 8). Activation energy increases first with conversion ratios, attains a maximum at ≈45% conversion and decreases afterwards. Similar values for activation energy were obtained for both KAS and FWO methods. The differential Friedman method yielded slightly lower values for activation energies. The activation energies calculated by FWO method falls between 1.3 and 2.1 eV. For nanocrystallites, as the reaction proceeds, reactants may undergo changes in reactivity due to crystal defect formation, intracrystalline strain and particle disintegration [16]. The reactivity of nickel nanocrystallites may not remain constant during the full course of the reaction. This may be the reason for the varying activation energies obtained at different conversions. However, the exact

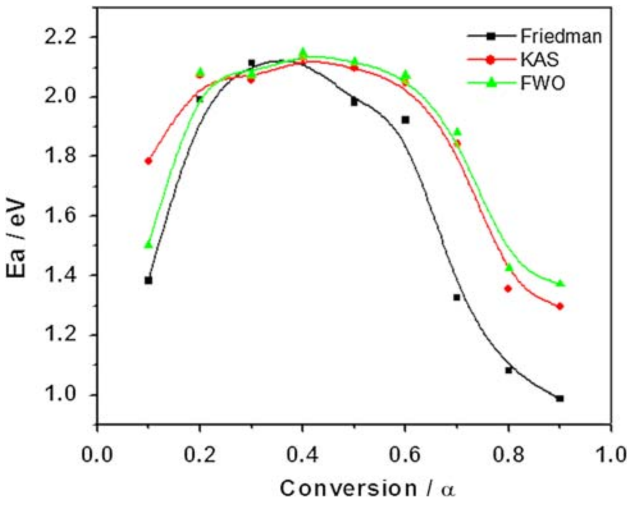

Fig. 8 Variation of activation energy with conversion for model free isoconversional equations

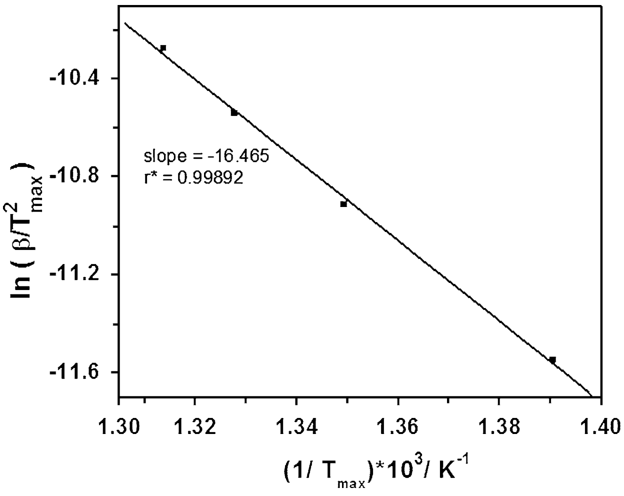

Fig. 9 Arrhenius plot using Kissinger equation

reason for a maximum in the curve could not be explained at this stage.

Kissinger equation [31] which yields a single value of activation energy was also used to determine the activation energy.

$$\ln\left(\frac{\beta}{T_{\max}^{2}}\right) = \ln\frac{AR}{E_a} - \frac{E_a}{RT_{\max}};$$

where $T_{\max}$ is the temperature of peak maximum from the DTG graph.

A plot of $\ln\left(\frac{\beta}{T_{\max}^{2}}\right)$ against $1/T_{\max}$ gives the Arrhenius (Fig. 9), plot from the slope of which activation energy can be determined.

The activation energy obtained was 136.8 kJ mol^{-1} (1.42 eV) which is within the range obtained by other methods.

Master plot method to study kinetics

To study the reaction kinetics of nickel oxidation we used the conventional master plot technique [32].

The $f(\alpha)/f(\alpha)_{0.5}$ were plotted for various differential $f(\alpha)$ functions against fractional conversion α. The experimental curve was plotted using variable activation energies obtained from FWO method and using the equation

$$\frac{f(\alpha)}{f(0.5)} = \frac{(\mathrm{d}\alpha/\mathrm{d}T)_{\alpha}\mathrm{e}^{\mathrm{Ea}/\mathrm{RT}_{\alpha}}}{(\mathrm{d}\alpha/\mathrm{d}T)_{0.5}\mathrm{e}^{\mathrm{Ea}/\mathrm{RT}_{0.5}}}.$$

The master plots of various differential functions and the experimental curve are shown in Fig. 10. Table 2 illustrates the various differential equations plotted in the master plot.

Unlike for the spherical nickel nano particles which generally obeys Jander equation [16] we got best fit for Johnson–Mehl–Avrami (JMA) equation of the form

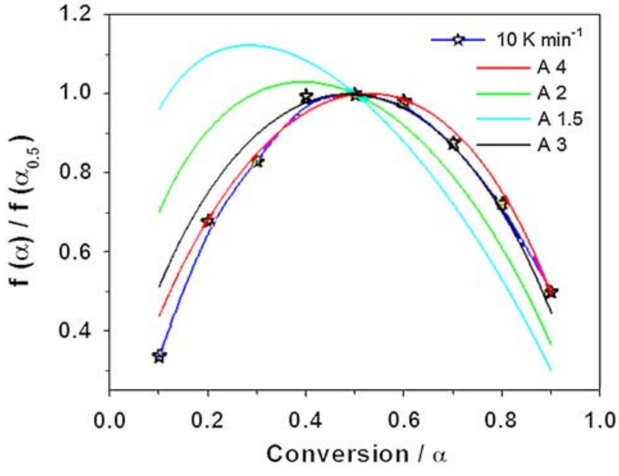

Fig. 10 Kinetic model fitting for nickel nano crystallites using differential equations in Table 2

Table 2 Differential equations of JMA kinetics with varying "*m*" values

Symbol	*f* (α)	*m*
A 1.5	$3/2(1-\alpha)[-\ln(1-\alpha)]^{1/3}$	1.5
A 2	$2(1-\alpha)[-\ln(1-\alpha)]^{1/2}$	2
A 3	$3(1-\alpha)[-\ln(1-\alpha)]^{2/3}$	3
A 4	$4(1-\alpha)[-\ln(1-\alpha)]^{3/4}$	4

$$f(\alpha) = m(1-\alpha)[-\ln(1-\alpha)]^{1-1/m}$$

where m is the Avrami exponent.

The equation with $m = 4$ gave best fit at conversion <0.5 while $m = 3$ gave good fitting for conversions >0.5. We suggest the film like morphology and the crystallite strain present on the sample should be the reason for this type of oxidation kinetics. Similar type of JMA kinetics was observed by Courtade et al. for the growth of NiO from Ni films [33]. As in our case, change in kinetics with lattice strain was recently reported for decomposition of ultrafine calcite by Ren et al. [34].

Conclusions

1. Controlled thermolysis of $[\mathrm{Ni(en)_2(H_2O)_2}](\mathrm{NO_3})_2$ in a static furnace at 200 °C resulted in formation of phase pure nickel nanocrystallites of average crystallite size 18.1 nm. The crystallites are agglomerated as indicated by SEM.
2. The thermolysis experiments indicated the autogenous temperature rise in the static furnace aided the formation of phase pure nickel. An increase in temperature or presence of extra oxygen directs the

reaction to form mixed phases of metallic nickel and nickel oxide in the TG experiments.

3. The nickel metal formed is of relatively high purity with a nitrogen rich species covering the surface. Due to this surface species nickel metal is resistant to oxidation at ambient temperatures.
4. Activation energy for nickel oxidation calculated by various methods shows a maximum around 45% conversion.
5. Johnson–Mehl–Avrami equation gave best fit with the experimental curve.
6. Activation energy of 1.42 eV/atom was obtained by the Kissinger method.

Acknowledgements The authors thank Department of Science and Technology, India for using the Sophisticated Analytical Instrument Facility (SAIF) at the Sophisticated Test and Instrumentation centre (STIC), Cochin University of Science and Technology, Cochin, for SEM analysis. S. Manju thanks Kerala State Council for Science, Technology and Environment for research fellowship.

References

1. Bruchez M, Moronne M, Gin P, Weiss S, Alivisatos AP. Semiconductor nanocrystals as fluorescent biological labels. Science. 1998;281:2013–6.
2. Kumar D, Zhou H, Nath TK, Kvit AV, Narayan J, Craciun V, et al. Improved magnetic properties of self-assembled epitaxial nickel nanocrystallites in thin-film ceramic matrix. J Mater Res. 2002;17:738–42.
3. Chu SZ, Wada K, Inoue S, Todoroki SI, Takahashi YK, Hono K. Fabrication and characteristics of ordered Ni nanostructures on glass by anodization and direct current electrodeposition. Chem Mater. 2002;14:4595–602.
4. Green M, O'Brien P. The preparation of organically functionalised chromium and nickel nanoparticles. Chem Commun 2001; 1912–3.
5. Yu K, Katabi G, Cao X, Prozorov R, Gedanken A. Sonochemical preparation of amorphous nickel. J Non-Cryst Solids. 1996;201: 159–62.
6. Degen A, Macek J. Preparation of submicrometer nickel powders by the reduction from nonaqueous media. Nano Struct Mater. 1999;12:225–8.
7. Davis SC, Klabunde KJ. Unsupported small metal particles: preparation, reactivity, and characterization. Chem Rev. 1982;82: 153–208.
8. Ni X, Zhao Q, Zhang D, Yang D, Zheng H. Large scaled synthesis of chainlike nickel wires assisted by ligands. J Cryst Growth. 2005;280:217–21.
9. Wang H, Jiao X, Chen D. Monodispersed nickel nanoparticles with tunable phase and size: synthesis, characterization, and magnetic properties. J Phys Chem C. 2008;112:18793–7.
10. Park J, Kang E, Son SU, Park HM, Lee MK, Kim J, et al. Monodisperse nanoparticles of Ni and NiO: synthesis, characterization, self-assembled superlattices, and catalytic applications in the Suzuki coupling reaction. Adv Mater. 2005;17:429–34.
11. Rejitha KS, Mathew S. Thermal deamination kinetics of tris(ethylenediamine)nickel(II) sulphate in the solid-state. J Therm Anal Calorim. 2008;93:213–7.
12. Schimpf S, Louis C, Claus P. Ni/SiO_2 catalysts prepared with ethylenediamine nickel precursors: influence of the pretreatment on the catalytic properties in glucose hydrogenation. Appl Catal A. 2007;318:45–53.
13. Negrier F, Marceau E, Che M, Giraudon JM, Gengembre L, Lofberg A. A systematic study of the interactions between chemical partners (metal, ligands, counterions, and support) involved in the design of Al_2O_3-supported nickel catalysts from diamine–Ni(II) chelates. J Phys Chem B. 2005;109:2836–45.
14. Atkinson A, Taylor RI. The diffusion of ^{63}Ni along grain boundaries in nickel oxide. Philos Mag A. 1981;43:979–98.
15. Zhou L, Rai A, Piekiel N, Ma X, Zachariah MR. Ion-mobility spectrometry of nickel nanoparticle oxidation kinetics: application to energetic materials. J Phys Chem C. 2008;112:16209–18.
16. Song P, Wen D, Guo ZX, Korakianitis T. Oxidation investigation of nickel nanoparticles. Phys Chem Chem Phys. 2008;10:5057–65.
17. Suwanwatana W, Yarlagadda S, Gillespie JW. An investigation of oxidation effects on hysteresis heating of nickel particles. J Mater Sci. 2003;38:565–73.
18. Karmhag R, Tesfamichael T, Wackelgard E, Niklasson GA, Nygren M. Oxidation kinetics of nickel particles: comparison between free particles and particles in an oxide matrix. Sol Energy. 2000;68: 329–33.
19. Negrier F, Marceau E, Che M, de Caro D. Role of ethylenediamine in the preparation of alumina-supported Ni catalysts from $[Ni(en)_2(H_2O)_2](NO_3)_2$: from solution properties to nickel particles. C R Chimie. 2003;6:231–40.
20. Suryanarayana C, Norton MG. X-ray diffraction a practical approach. New York: Plenum Press; 1998.
21. Curtis NF, Curtis YM. Some nitrato-amine Nickel(II) compounds with monodentate and bidentate nitrate ions. Inorg Chem. 1965;4: 804–9.
22. Nakamoto K. Infrared and Raman spectra of inorganic and coordination compounds part B: applications in coordination, organometallic, and bioinorganic chemistry. 5th ed. New York: Wiley; 1997.
23. Sun KQ, Marceau E, Che M. Evolution of nickel speciation during preparation of Ni–SiO_2 catalysts: effect of the number of chelating ligands in $[Ni(en)_x(H_2O)_{6-2x}]^{2+}$ precursor complexes. Phys Chem Chem Phys. 2006;8:1731–8.
24. JCPDS card No: 04-0850.
25. Guerlou GL, Delmas C. Structure and properties of precipitated nickel-iron hydroxides. J Power Sour. 1993;45:281–9.
26. JCPDS card No: 47-1049.
27. Karmhag R, Niklasson GA, Nygren M. Oxidation kinetics of nickel nanoparticles. J Appl Phys. 2001;89:3012–7.
28. Flynn JH, Wall LA. A quick, direct method for the determination of activation energy from thermogravimetric data. J Polym Sci B. 1996;4:323–8.
29. Akahira T, Sunose T. Research report of Chiba Institute Technology. 1971;16:22.
30. Friedman HL. New methods for evaluating kinetic parameters from thermal analysis data. J Polym Sci B. 1969;7:41–6.
31. Kissinger HE. Reaction kinetics in differential thermal analysis. Anal Chem. 1957;29:1702–6.
32. Gotor FJ, Criado JM, Malek J, Koga N. Kinetic analysis of solid-state reactions: the universality of master plots for analyzing isothermal and nonisothermal experiments. J Phys Chem A. 2000;104: 10777–82.
33. Courtade L, Turquat Ch, Muller Ch, Lisoni JG, Goux L, Wouters DJ, et al. Oxidation kinetics of Ni metallic films: formation of NiO-based resistive switching structures. Thin Solid Films. 2008; 516:4083–92.
34. Ren YL, Wang X, Shui M, Li RS. The influence of morphology of ultra-fine calcite particles on decomposition kinetics. J Therm Anal Calorim. 2008;91:867–71.